



Cite this: *Phys. Chem. Chem. Phys.*,  
2018, 20, 28144

# Electronic spectrum and characterization of diabatic potential energy surfaces for thiophenol†

Linyao Zhang,<sup>id</sup> ab Donald G. Truhlar,<sup>id</sup> \*b and Shaozeng Sun\*<sup>a</sup>

The electronic spectrum of thiophenol was simulated by a normal-mode sampling approach combined with TDDFT in the Tamm–Dancoff approximation (TDA). The vertical excitation energies were compared with electronic structure calculations by completely renormalized equation-of-motion coupled cluster theory with single and double excitations and noniterative inclusion of connected triples (CR-EOM-CCSD(T)) and by multi-reference perturbation theory. The spectrum was computed both with and without solvation effects, and these spectra are compared to each other and to experiment. Using multireference-perturbation-theory adiabatic wave functions and model-space diabaticization by the fourfold way, diabatic potential energy surfaces of the lowest three singlet states ( $^1\pi\pi$ ,  $^1\pi\pi^*$ , and  $^1n_\pi\sigma^*$ ) were constructed along the S–H stretching coordinate, the C–C–S–H torsion coordinate, and the  $v_{16a}$  and  $v_{16b}$  normal coordinates. The first two of these two are primary coordinates for the photodissociation, and the diabatic crossing seams of the three states were calculated and plotted as functions of the two coordinates. The other two coordinates are out-of-plane ring distortion modes studied to assess the extent of their role in coupling the states near the first conical intersection, and the  $v_{16a}$  mode was shown to be an important coupling mode there. The current study is the first step toward a detailed mechanistic analysis of the photoinduced S–H fission process of thiophenol, a test system to understand  $^1n_\pi\sigma^*$ -mediated reactions, at the same time already providing a better understanding of the thiophenol electronic excitations by clarifying the assignment of the experimental results.

Received 15th August 2018,  
Accepted 24th October 2018

DOI: 10.1039/c8cp05215h

rsc.li/pccp

## 1. Introduction

Sobolewski, Domcke, and coworkers<sup>1–4</sup> showed that the optically dark and repulsive excited singlet states of  $^1n_\pi\sigma^*$  character, which can intersect with bound  $^1\pi\pi^*$  states and the ground states, play a pivotal role in photoinduced hydrogen detachment processes for a variety of molecules. As reviewed by Ashfold and coworkers, these states have now been widely studied because of their prominence in many photodissociation processes, especially those of biological importance.<sup>5,6</sup> The photoinduced S–H fission process in thiophenol ( $C_6H_5SH$ ) can serve as a test system to understand such  $^1n_\pi\sigma^*$ -mediated reactions.

Photodissociation of thiophenol produces thiophenoxy radicals in two close-lying states, namely the ground state,  $\tilde{X}^2B_1$ , and the first excited state,  $\tilde{A}^2B_2$ . These two states differ in the orbital orientation of the singly occupied molecular orbital (SOMO) with respect to the aromatic ring. Kim, Lee, and

coworkers<sup>7–9</sup> measured the relative yields of these states by velocity map ion imaging experiments with thiophenol- $d_1$  ( $C_6H_5SD$ ) pumped at 266, 243, and 224 nm (4.66, 5.10, and 5.54 eV). Although, extensive experimental and theoretical work has been reported on the photoinduced dissociation dynamics of thiophenol and its derivatives,<sup>7–23</sup> detailed reaction mechanisms in terms of the intermediate states are yet to be fully developed.

A detailed mechanistic study of the photoinduced S–H fission process requires nonadiabatic dynamics simulations governed by reliable potential energy surfaces (PESs) and their couplings. Understanding the excitations and validating the methods used to calculate them is the first step toward a dynamics simulation of the photodissociation. The ultraviolet (UV) absorption spectrum of thiophenol, taken in *n*-hexane,<sup>8,9</sup> has a strong peak at around 234 nm (5.30 eV). In order to have a better understanding of the excitations that contribute to the spectrum, we have simulated the spectrum using the normal-mode sampling strategy that has previously been used successfully for the study of thioanisole.<sup>24</sup>

To proceed toward dynamics, one must consider not just vertical excitations but also global potential energy surfaces and couplings. We study these here by working out the nature of the underlying diabatic states. Breakdown of the Born–Oppenheimer (BO) approximation<sup>25</sup> couples the electronic and nuclear motion

<sup>a</sup> School of Energy Science and Engineering, Harbin Institute of Technology, Harbin 150001, P. R. China. E-mail: sunsz@hit.edu.cn

<sup>b</sup> Department of Chemistry, Chemical Theory Center, and Supercomputing Institute, University of Minnesota, Minneapolis, Minnesota 55455, USA. E-mail: truhlar@umn.edu

† Electronic supplementary information (ESI) available. See DOI: 10.1039/c8cp05215h

during photodissociation and leads to nonadiabatic transitions. Along paths near seams of conical intersections, the adiabatic energy gap (difference in energy of two adiabatic electronic states) goes through a local minimum (called a locally avoided crossing),<sup>26</sup> and the adiabatic electronic states change their character rapidly; nonadiabatic transitions often occur in such seam neighborhoods.<sup>27</sup> The process can often be understood more easily by using diabatic electronic states that change smoothly and cross in such regions.<sup>28–30</sup> Furthermore, the state couplings in the Born–Oppenheimer adiabatic representation are vectors with singularities at conical intersections and unphysical behavior in some dissociation limits,<sup>31</sup> which can make them inconvenient for dynamics simulations, whereas the couplings in the diabatic representation are smooth scalars, and the flexibility of diabatic representations<sup>32</sup> can be used to make the couplings physical in asymptotic regions. (The diabatic potential energy surfaces are the diagonal elements of the Hamiltonian in the diabatic representation, and the diabatic couplings are the scalar off-diagonal elements of the Hamiltonian in the diabatic representation.) Therefore, we will study diabatic representations as the next step in exploring the mechanism.

Diabatic representations are not unique, and there is great flexibility in finding suitable ones, with the main criterion being that the electronic wave functions and diabatic matrix elements are smooth functions of internuclear distance.<sup>32</sup> In many cases the diabatic states have simple interpretations in valence bond language.<sup>29,31,33–39</sup> In the present study, we calculate the diabatic states using the fourfold way<sup>40–43</sup> starting with complete-active-space self-consistent-field<sup>44,45</sup> (CASSCF) adiabatic wave functions and using a model space diabatization scheme<sup>46</sup> to get more accurate diabatic potentials and couplings by (extended) multi-configuration quasi-degenerate perturbation theory<sup>47–49</sup> ((X)MC-QDPT).

For the adiabatic states of thiophenol we consider the ground state ( $S_0$ ) and the first three excited singlet states ( $S_1$ ,  $S_2$ , and  $S_3$ ). We also consider the two lowest adiabatic states of thiophenoxyl radical ( $D_0$  and  $D_1$ ). We study the diabatic potentials as functions of four coordinates. First the dissociative S–H distance  $R$  and the C–C–S–H torsion angle  $\phi$  were singled out as primary coordinates, as in an earlier study of the diabatic potentials of phenol<sup>50</sup> using the anchor points reactive potential<sup>51</sup> (APRP) method. Second we studied two out-of-plane ring distortion modes, in particular normal coordinates  $\nu_{16a}$  and  $\nu_{16b}$  (labeled according to ref. 52), which are out-of-plane ring distortion modes.

## 2. Computational methods

### 2.1 Adiabatic calculations

We used both Kohn–Sham density functional theory (KS-DFT) and wave function theory (WFT) in the present study. For DFT we employed – at various places along the way – five exchange–correlation functionals: M06-2X,<sup>53</sup>  $\tau$ -HCTHhyb,<sup>54</sup> M06-L,<sup>55</sup> MN15,<sup>56</sup> and B3LYP.<sup>57–60</sup> Four basis sets were employed, in particular, minimally augmented-multiply polarized valence

triple zeta (MG3S),<sup>61</sup> augmented correlation-consistent polarized valence triple zeta (aug-cc-pVTZ),<sup>62,63</sup> aug-cc-pVTZ with an additional tight d function for sulfur atom (aug-cc-pV(T+d)Z),<sup>64</sup> and the Karlsruhe triple zeta valence polarized basis set (def-TZVP).<sup>65</sup>

The  $S_0$  equilibrium geometry of thiophenol and the  $D_0$  equilibrium geometry of thiophenoxyl radical were optimized by M06-2X/aug-cc-pVTZ. We studied the vertical excitation energies and the S–H bond dissociation energy with these ground-state geometries except where specified otherwise. The methods used for vertical excitation energy are (i) linear-response time-dependent density functional theory (TDDFT)<sup>66</sup> with MN15 and B3LYP and TDDFT using the Tamm–Dancoff approximation<sup>67–69</sup> (TDA-TDDFT) with  $\tau$ -HCTHhyb; (ii) multi-configurational quasi-degenerate perturbation theory<sup>47,48</sup> (MC-QDPT) and its extended version<sup>49</sup> (XMC-QDPT); (iii) equation-of-motion coupled cluster theory with singles and doubles<sup>70,71</sup> (EOM-CCSD), and (iv) completely-renormalized equation-of-motion coupled cluster theory with singles, doubles, and non-iterative connected triples<sup>72,73</sup> (CR-EOM-CCSD(T)).

CASSCF calculations (or, more generally, multi-configurational self-consistent field (MCSCF) calculations) include static correlation and inevitably also some dynamic correlation; the remainder of the dynamic correlation is called<sup>74</sup> external correlation. To include external correlation, both MC-QDPT and XMC-QDPT calculations (denoted as QDPT when we are referring to both kinds of calculation) were performed based on a state-averaged CASSCF<sup>44,45</sup> reference states, which are averaged over three states or four states and which include 12 active electrons and 11 active orbitals; the notation for these calculations is SA(3)-CASSCF or SA(4)-CASSCF. The active orbitals from such a calculation are shown in Fig. 1. QDPT calculations based on SA(3)-CASSCF have a three-state model space and are denoted as QDPT(3); QDPT calculations based on SA(4)-CASSCF have a four-state model space and are denoted as QDPT(4).

Solvent effects were considered by applying the SMD model<sup>75</sup> for solvent radii and using the integral equation formalism<sup>76,77</sup> to solve the nonhomogeneous-dielectric Poisson equation for the electrostatics. Solvent effects on excitation energies were treated using the excited-state relaxed density matrix and the state-specific corrected linear response (cLR) approximation.<sup>78</sup>

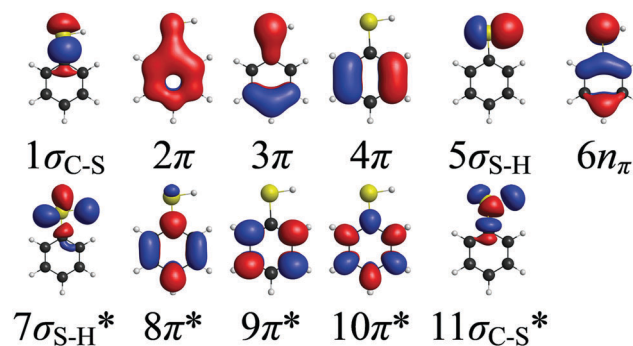


Fig. 1 The eleven SA(3)-CASSCF canonical active orbitals at the  $S_0$  equilibrium geometry with  $C_s$  symmetry ( $R = 1.338$  Å and  $\phi = 0^\circ$ ).

For the purpose of geometry optimization and zero-point energy calculations, we also performed state-specific versions of CASSCF, again with 12 electrons in 11 orbitals; these are denoted as SS. The adiabatic excitation energy for the  $S_1 \leftarrow S_0$  excitation is calculated with the following formula:<sup>24</sup>

$$\Delta E(S_1 \leftarrow S_0) = V_e(S_1) + ZPE(S_1) - V_e(S_0) - ZPE(S_0) \quad (1)$$

where  $V_e(S_i)$  ( $i = 0, 1$ ) is the electronic energy of the  $S_i$  state calculated by XMC-QDPT/MG3S at the  $S_i$  minimum geometry optimized by SS/MG3S, and  $ZPE(S_i)$  is the zero-point energy of  $S_i$  calculated by SS/MG3S.

## 2.2 Simulation of electronic absorption spectrum

The absorption spectrum of thiophenol has been simulated following the same strategy as used previously<sup>24</sup> for the study of thioanisole, in particular by averaging over a number of geometries generated according to the ground-state vibrational distribution. This involves four steps. First, we optimized the ground-state geometry of thiophenol and performed normal mode analysis by M06-L/def-TZVP in the gas phase. Then 200 geometries were sampled with the ground-state harmonic oscillator distribution along each Cartesian normal coordinate. Third, the vertical excitation energies and oscillator strengths of the four lowest excited states were calculated for each sampled geometry using TDA- $\tau$ -HCTHhyb/def-TZVP/SMD/cLR, and both the gas-phase and solvent-phase results were used to generate spectra by applying Gaussian broadening with a 0.2 eV half width at half maximum (HWHM). Finally, spectra were averaged over the ensemble of 200 geometries.

## 2.3 Fourfold way and model space diabaticization

In a recent study, reduced-dimensionality diabatic potential energy surfaces have been obtained<sup>22,23</sup> for thiophenol using the linear-vibronic coupling model,<sup>79,80</sup> which is designed to remove only the singular couplings at or near conical intersections by using information only about the adiabatic potentials. In the present study we apply the fourfold way, which is designed to yield globally valid diabaticizations by using information about the orbitals and configuration state functions (CSFs) as well as the adiabatic potentials.

The fourfold way<sup>40–43</sup> is a general, path-independent diabaticization scheme based on configurational uniformity<sup>81</sup> for calculating diabatic states and their scalar couplings such that the diabatic states span the same space as selected adiabatic states. The fourfold way was originally formulated at the CASSCF level<sup>40</sup> and then extended to the QDPT level<sup>41</sup> with DMOs obtained either by QDPT level<sup>41</sup> or by CASSCF.<sup>43</sup> The fourfold way was designed to be adiabatic-equivalent; that is, if  $n$  diabatic states are considered, they should span the same space as the  $n$  lowest adiabatic states at each geometry. Then, when one diagonalizes the diabatic Hamiltonian, one obtains back the original adiabatic states. In the original versions of the method, this is usually true to a good approximation, but the adiabatic energies (and hence the external correlation energies) are not quite the same as the energies of

the variationally optimized adiabatic states due to lack of invariance of these states to orbital rotations in standard programs. In the final version of the fourfold way, called the model space version,<sup>46</sup> this problem is removed so that external correlation is included by standard post-MCSCF multi-state methods (with the variationally optimized orbitals) even though the diabaticization is based on state-averaged MCSCF results. Detailed theory and algorithms of the fourfold-way<sup>40–43</sup> and model-space scheme<sup>46</sup> are presented in our original and subsequent work;<sup>82,83</sup> here we only summarize the key concepts for generating the diabatic surfaces of thiophenol.

As the usual canonical MOs (CMOs) generated from SA-CASSCF procedure often change character along nuclear coordinates due to avoided crossing, using them does not generate smooth CSFs. Therefore the first step is to construct smoothly varying diabatic molecular orbitals (DMOs) and then re-express the CSFs in terms of these new DMOs to make the CSFs be smooth functions of geometry. The DMOs in the active space are obtained from an orthogonal transformation of the active CMOs by applying the threefold density criterion and, when needed, a fourth criterion of maximum overlap of reference MOs (MORMO). For the thiophenol photodissociation involving multiple nonbonding p orbitals, the threefold density criterion is insufficient to generate smoothly changing DMOs (as found previously for phenol)<sup>82</sup> and thus we need to employ the MORMO criterion by using one or more additional reference orbitals.

For the present case, we use standard parameter values<sup>40</sup> for the threefold density functional and include only one reference MO. The choice of reference MO or MOs is important, but not necessarily intuitive; it is usually sufficient to include one or both of any degenerate or nearly degenerate MOs that are localized on one or a small number of atoms. In the present work we therefore took the in-plane  $n(p_y)$  orbital be a reference MO, and we found that one reference MO is sufficient. Although the choice of reference orbitals will influence the resulting diabatic states to some extent, physically similar choices will generate qualitatively similar results. Nevertheless we note that our specific choice was to evaluate the reference MO on sulfur at a geometry with an S–H distance equal to 5 Å; the shape of the reference MO is shown in Fig. 2.

The second step is to construct a list of prototype CSFs for each diabatic state used to produce smooth diabatic surfaces. These diabatic prototype CSFs are chosen from the most

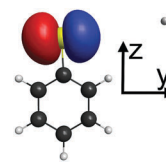


Fig. 2 The MORMO reference orbital used in current fourfold-way calculation. The thiophenoxyl radical is in the  $yz$  plane with the  $z$ -axis along the C–S bond.

Table 1 Prototype list<sup>a</sup>

Prototype CSFs for diabatic state  $\phi_1$

$\chi_1^1$ : 222212 10000

Prototype CSFs for diabatic state  $\phi_2$

$\chi_2^1$ : 222221 00100

$\chi_2^2$ : 222122 01000

$\chi_2^3$ : 222122 10000

$\chi_2^4$ : 222220 11000

Prototype CSFs for diabatic state  $\phi_3$

$\chi_3^1$ : 222222 00000

$\chi_3^2$ : 222221 10000

<sup>a</sup> CSFs are defined by the occupancies of the 11 DMOs in Fig. 1 in the same order.

important CSFs of each adiabatic state at some potential reference geometries in weak-interaction regions where adiabatic states are, to a good approximation, the same as diabatic states. Among the criteria to be fulfilled when building the prototype CSFs list is that a CSF cannot appear in the list of more than one diabatic state; a more complete explanation of the requirements for prototype CSFs list can be found in our original<sup>40–43</sup> and subsequent<sup>82,83</sup> papers. We determined the prototype list by examining the leading CSF coefficients at many geometries, and the final list used for the present application is specified in Table 1.

Once the diabatic prototypes are specified, an adiabatic to diabatic orthogonal transformation is performed to construct the diabatic states from adiabatic states for all geometries. The transformation matrix is obtained by configurational uniformity approach with the criterion of maximizing the projection of the adiabatic CSFs onto the selected prototype CSFs.

To obtain diabatic energies at QDPT level (in present study we use XMC-QDPT energies), we first perform the fourfold-way at the CASSCF level and standard XMC-QDPT calculations, separately. Then the necessary information is extracted from standard GAMESS output for the model space diabaticization scheme, which involves only matrix transposes and multiplications.

## 2.4 Details

All the KS-DFT, TDDFT and TDA-TDDFT calculations were performed using *Gaussian 16*,<sup>84</sup> with an ultrafine (99, 590) grid for numerical integration except for the  $\tau$ -HCTHhyb functional for which used a fine (75, 302) grid; all the CASSCF, SA-CASSCF and QDPT calculations were carried out within *GAMESS*<sup>85</sup> by using equal weights for each states for all state-average calculations and an intruder state avoidance<sup>86</sup> with an energy denominator shift of  $0.02E_h$  for QDPT calculations; all EOM-CCSD and CR-EOM-CCSD(T) calculations were carried out by *NWChem*<sup>87</sup> without correlating the core orbitals of the atoms (the 1s orbitals on H and C and the 1s, 2s, and 2p orbitals on S).

Averaging of the spectrum over the ground-state vibrational distribution was carried out using *ANT*<sup>88</sup> interfaced with *Gaussian 16*. *Multwfn*<sup>89</sup> was used to perform the Gaussian broadening.

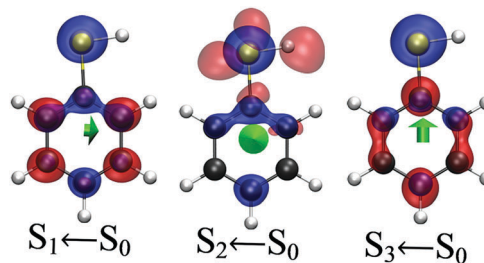


Fig. 3 Hole (blue) and particle (red) distributions due to the excitations and the total transition dipole moment vector of gas-phase thiophenol from TDA- $\tau$ -HCTHhyb/def-TZVP calculations at the M06-2X/aug-cc-pVTZ  $S_0$  equilibrium geometry, where the  $n_\pi\sigma^*$  transition is perpendicular to the molecular plane and the two  $\pi\pi^*$  transitions are parallel to the molecular plane with angles of  $14.0^\circ$  and  $80.5^\circ$  relative to the S–H bond axis.

## 3. Results and discussion

### 3.1 Nature of the four lowest singlet states and electronic spectroscopy

For the photodissociation of thiophenol with excitation energies in the range up to 5.5 eV, as involved in the experiments,<sup>7,8,10,18</sup> only the two lowest excited singlet states ( $S_1$  and  $S_2$ ) are important. However, the third excited singlet state ( $S_3$ ) makes an important contribution to the electronic spectrum, so the four lowest singlet states are considered in this section. The ground state ( $S_0$ ) of thiophenol at the equilibrium geometry with  $C_s$  symmetry is a closed-shell state belonging to the  $A'$  irreducible representation (irrep), the first ( $S_1$ ) and third ( $S_3$ ) excited states are  $1\pi\pi^*$  states belonging to the  $A'$  irrep, and the second excited state ( $S_2$ ) is a  $1n_\pi\sigma^*$  state belonging to the  $A'$  irrep. Both  $S_1$  and  $S_3$  have some  $1n_\pi\pi^*$  character, which may be attributed to the strongly delocalized character of the 3p valence orbital of the sulfur atom. But, for convenience we just label them as  $1\pi\pi^*$  to be consistent with labeling used by other authors.<sup>16,18</sup>

The vertical excitation energies of thiophenol and thiophenoxy as well as the S–H bond dissociation energy to the  $\tilde{X}^2B_1$  state of thiophenoxy are summarized in Table 3 as calculated by variety of electronic structure methods. It can be seen that XMC-QDPT and CR-EOM-CCSD(T) give very similar results with the large aug-cc-pV(T+d)Z basis set, which suggests that the results from these two very different kinds of high-level methods should both be reliable. When using the smaller MG3S basis set, XMC-QDPT can also give accurate results for both 3-state-averaged and 4-state-averaged calculations. The calculated bond dissociation energies with the various methods are all in good agreement with the experimental ones,<sup>7,8,10,16,18</sup> which are in the range of 3.33 to 3.62 eV. We also calculated the  $S_1 \leftarrow S_0$  adiabatic excitation energy using eqn (1), which is 4.28 eV in excellent agreement with the experimental values of 4.27<sup>16</sup> and 4.34<sup>18</sup> eV.

The hole and particle distributions for the first three excited states of thiophenol as obtained by the TDA- $\tau$ -HCTHhyb method are visualized by the *Multwfn* software<sup>89</sup> with the results shown in Fig. 3. The hole and particle distributions of the three excitations clearly show the importance of the sulfur's  $n(p_y)$  orbital (the  $n_\pi$  orbital of the molecule), in agreement with

**Table 2** The CI coefficients of the dominant configurations of the four lowest singlet states of gas-phase thiophenol at the  $S_0$  equilibrium geometry<sup>a</sup> as calculated by SA(4)-CASSCF/MG3S

State <sup>b</sup>	Dominant configuration (s) <sup>c</sup>	CI coefficient
$S_0$	222222 00000	0.93
$S_1$	222221 00100	0.63
	222122 01000	0.59
$S_2$	222221 10000	0.84
	221222 10000	0.35
$S_3$	222221 01000	0.86
	221222 01000	0.23

<sup>a</sup> Geometry optimized by M06-2X/aug-cc-pVTZ. <sup>b</sup> These state labels apply globally to the diabatic states, but they also apply approximately to the adiabatic states at the ground-state equilibrium geometry. <sup>c</sup> The occupation numbers of the dominant configurations correspond to orbitals in Fig. 1 in the same order.

our CASSCF results (see the dominant configurations of each state in Table 2). This also suggests that the WFT and KS-DFT methods can give consistent results. The oscillator strengths and transition dipole moments can also be used to understand the nature of transitions. All of these transitions are allowed by symmetry (similar to the situation studied previously in thioanisole<sup>24</sup>). As seen in Table 4, all methods (EOM-CCSD, TDDFT, and, SA-CASSCF) predict qualitatively similar results, in particular a large oscillator strength for the second  $^1\pi\pi^*$  transition ( $S_3 \leftarrow S_0$ ), a small oscillator strength of the first  $^1\pi\pi^*$  transition ( $S_1 \leftarrow S_0$ ), and a negligibly small oscillator strength for the  $^1n_\pi\sigma^*$  transition ( $S_2 \leftarrow S_0$ ). The total transition dipole moment of the  $^1n_\pi\sigma^*$  transition calculated at the optimized  $S_0$  geometry is perpendicular to the molecular plane, whereas those of the first and second  $^1\pi\pi^*$  transitions are in the molecular plane. The green arrows in Fig. 3 depict the orientation of the transition dipole moment calculated at TDA- $\tau$ -HCTHhyb/def-TZVP level, and the angles with respect to the S-H bond axis for the first and second  $^1\pi\pi^*$  transitions are  $14.0^\circ$  and  $80.5^\circ$ , respectively.

From the above analysis we see that the TDA- $\tau$ -HCTHhyb density functional with the small def-TZVP basis set predicts the vertical excitation energies very close to our best estimates,

**Table 4** Gas-phase oscillator strengths from various calculations<sup>a</sup>

Method	Basis set	$S_1(2A')$ $^1\pi\pi^*$	$S_2(1A'')$ $^1n_\pi\sigma^*$	$S_3(3A')$ $^1\pi\pi^*$
EOM-CCSD	aug-cc-pV(T+d)Z	0.0047	0.0028	0.2406
TD-MN15	MG3S	0.0126	0.0005	0.2246
TD-B3LYP	MG3S	0.0120	0.0018	0.2226
TDA- $\tau$ -HCTHhyb	def-TZVP	0.0149	0.0001	0.2713
SA(4)-CASSCF	MG3S	0.0002	0.0000	0.3877

<sup>a</sup> The geometry used are  $S_0$  equilibrium geometries optimized at M06-2X/aug-cc-pVTZ level.

and the oscillator strengths also close to those obtained with the other two functionals. Although the ratio of the  $S_1 \leftarrow S_0$  to  $S_2 \leftarrow S_0$  oscillator strength obtained from EOM-CCSD is smaller than the ratio obtained with TDDFT, the absolute values of these two oscillator strengths are relatively small, and the following analysis also shows that the third transition is the most important one for reproducing the unresolved absorption band shape in the wavelength range from 220 to 300 nm. Considering its computational efficiency and accuracy, the TDA- $\tau$ -HCTHhyb/def-TZVP method was selected for our spectral simulations.

To mimic the experimental absorption spectrum, we need to broaden the discrete excitation sticks with functions that simulate the Franck-Condon broadening over and above that included by our averaging over the initial vibrational motions. The Gaussian and Lorentzian functions are both extensively used for simulating electronic absorption spectra, but the Gaussian form is more commonly used.<sup>90</sup> We tried several different half-width-at-half-maximum (HWHM) parameters, and we found Gaussian broadening with HWHM = 0.2 eV provides a good fit to the overall band shape (see Fig. S1 and S2 in the ESI†). Fig. S3 in the ESI† also shows results by applying Lorentzian broadening with HWHM = 0.2 eV, and it can be seen that the profiles predicted with the Lorentzian function are less satisfactorily in the long wavelength tail, and therefore we did not use the Lorentzian function.

As shown in Fig. 4 (adapted from ref. 8), the experimental electronic spectrum of thiophenol taken in *n*-hexane shows a

**Table 3** Gas-phase vertical excitation energies (VEEs) of thiophenol and thiophenoxyl and the S-H bond dissociation energy (BDE) to the  $\tilde{X}^2B_1$  state of the thiophenoxyl (in eV) as calculated by different methods and basis sets<sup>a</sup>

Method	Basis set	PhSH VEE			PhS* VEE $\tilde{X}^2B_1-\tilde{A}^2B_2$	BDE
		$S_1(2A')$	$S_2(1A'')$	$S_3(3A')$		
CR-EOM-CCSD(T)	aug-cc-pV(T+d)Z	4.57	4.95	5.44	0.19	3.66
EOM-CCSD	aug-cc-pV(T+d)Z	4.89	5.15	5.73	0.35	3.66
TD-MN15	MG3S	4.95	5.00	5.40	0.10	3.65
TD-B3LYP	MG3S	4.76	5.15	5.52	0.39	3.63
TDA- $\tau$ -HCTHhyb	def-TZVP	4.79	5.07	5.44	0.41	3.63
XMC-QDPT(4)	aug-cc-pV(T+d)Z	4.59	5.10	5.31	0.23 <sup>b</sup>	3.63 <sup>b</sup>
XMC-QDPT(4)	MG3S	4.62	5.14	5.38	0.23 <sup>b</sup>	3.53 <sup>b</sup>
XMC-QDPT(3)	aug-cc-pV(T+d)Z	4.58	5.03	—	0.27 <sup>b</sup>	3.60 <sup>b</sup>
XMC-QDPT(3)	MG3S	4.62	5.07	—	0.27 <sup>b</sup>	3.51 <sup>b</sup>
Expt.		4.34 <sup>c</sup>	4.59 <sup>c</sup>	—	0.32–0.37 <sup>e</sup>	3.33–3.62 <sup>e</sup>
		4.27 <sup>d</sup>	4.51 <sup>d</sup>	—		

<sup>a</sup> The geometries of thiophenol and thiophenoxyl used in these calculations are  $S_0$  equilibrium geometries optimized at M06-2X/aug-cc-pVTZ level, unless specified otherwise. <sup>b</sup> Values for PhS\* are calculated using optimized PhS\* geometry with a H atom putting at the distance of  $R_{S-H} = 20$  Å. <sup>c</sup> From ref. 18. <sup>d</sup> From ref. 16. <sup>e</sup> From ref. 7, 8, 10, 16 and 18.

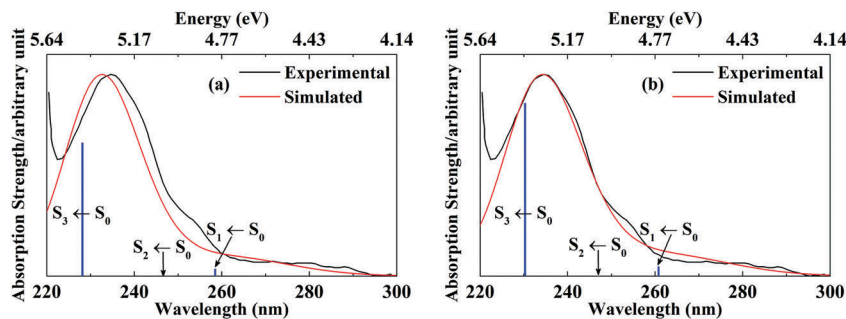


Fig. 4 Experimental absorption spectrum taken in *n*-hexane (data from Fig. 5 of ref. 8) and simulated spectra with vertical excitation energies and oscillator strengths calculated by TDA- $\tau$ -HCTHhyb/def-TZVP: (a) gas-phase simulation; (b) liquid-phase simulation using TDA- $\tau$ -HCTHhyb/def-TZVP with state-specific corrected linear response for solvation effects with the SMD solvation model in *n*-hexane, and broadened using Gaussian function with HWHM = 0.2 eV.

strong absorption peak at around 234 nm (5.30 eV) and a long wavelength tail with no discernible structure, as shown in Fig. 4. Fig. 4 (and Fig. S3 in the ESI†) show that solvation effects on the spectrum are small but not completely negligible even in the nonpolar solvent. From our calculated vertical excitation energies we conclude that the second  $^1\pi\pi^*$  ( $S_3 \leftarrow S_0$ ) transition (5.39 eV) should be responsible for the strong peak. This is consistent with the general conclusion in Ferrer *et al.*<sup>90</sup> that the maximum in the absorption spectrum is expected to be red-shifted ( $\sim 0.1$  to  $0.3$  eV) as compared to the relevant vertical excitation energy. In order to further verify our understanding of the spectrum as well as the nature of each excitation mode, we simulated the spectrum using the normal-mode sampling method as describe above and in our previous study.<sup>24</sup> We mainly focus on the first three lowest excited states, but we used the first four excitations to produce the spectrum. The simulations are compared to experiment in Fig. 4. The simulated profile in the gas phase, Fig. 4a, shows an overall shift ( $\sim 0.04$  eV) with respect to the experimental result, but the profile generated with data from the SMD/cLR solvent model is in excellent agreement with experiment. Although not an unexpected result, it seems worthwhile to point out that the peak in the unresolved experimental spectrum does not provide a good measure of any of the vertical excitation energies. We emphasize that the goal of our normal-mode sampling approach for simulating the spectrum is to make the simulation more realistic and less arbitrary, but higher accuracy in modeling the spectrum would require the use of excited-state gradients,<sup>24</sup> which were not calculated in the present study.

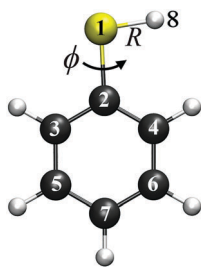


Fig. 5 The two degrees of freedom considered in this study: S-H(8) distance  $R$  and C(4)-C(2)-S-H(8) torsion angle  $\phi$ .

### 3.2 Diabatic potential energy surfaces

Two of the disappearing coordinates during the photodissociation process, the S-H fission coordinate  $R$  and the C-C-S-H torsion angle  $\phi$ , are shown in Fig. 5. In what follows, we

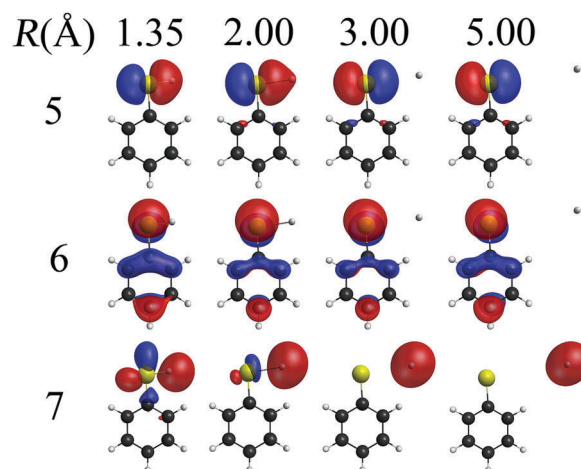


Fig. 6 Diabatic MOs (5, 6, and 7) at several  $R$  with  $\phi = 0^\circ$ .

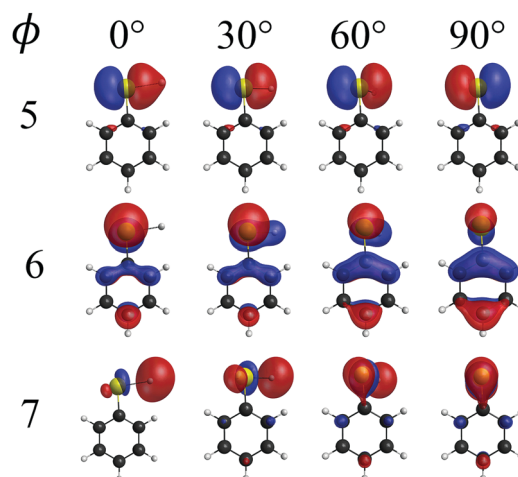


Fig. 7 Diabatic MOs (5, 6, and 7) space at several  $\phi$  with  $R = 2.00$  Å.

consider the fifth, sixth, and seventh DMOs (numbered to approximately match the CMOs in Fig. 1 in the same order) and the potential energy surfaces of the lowest three singlet states as functions of each of these coordinates with all other geometric parameters fixed at the  $S_0$  equilibrium geometry.

For the fourfold-way diabaticization calculations, the first step is to construct smoothly varying DMOs using the threefold density criterion and the  $n(p_y)$  orbital of sulfur as a MORMO reference orbital. Fig. 6 and 7 depict three of the DMOs. We can see that they change smoothly as functions of geometry along the two selected coordinates. Based on the smooth DMOs and the prototype list of Table 1, we obtained smooth diabatic potential and coupling curves along the  $R$  and  $\phi$  coordinates as shown in Fig. 8.

Fig. 8 clearly shows two conical intersections (CIs) along  $R$  with  $C_s$  symmetry (planar geometries with  $\phi = 0^\circ$ , Fig. 8a). For planar geometries, the diabatic potential energy curves match the adiabatic curves in energy with essentially zero diabatic couplings; the  $^1\pi\pi^*/^1n_\pi\sigma^*$  CI is at  $R \cong 1.45 \text{ \AA}$ , which is very close to the  $^1\pi\pi^*$  energy minimum, and the  $^1\pi\pi/^1n_\pi\sigma^*$  CI is at  $R \cong 3.0 \text{ \AA}$ .

For geometries with  $\phi$  fixed at  $90^\circ$  (Fig. 8d), the diabatic curves are also energetically similar to the adiabatic ones with negligible couplings, but only the  $^1\pi\pi^*$  and  $^1n_\pi\sigma^*$  states cross. Since the electronic structure of the thiophenoxyl moiety is independent of  $\phi$  for very large  $R$ , and since the diabatic states  $^1\pi\pi^*$  and  $^1\pi\pi$  cross along  $R$  at  $\phi = 0^\circ$  but not at  $\phi = 90^\circ$ , it is clear that these states must cross along  $\phi$  at small  $R$ . And this is true

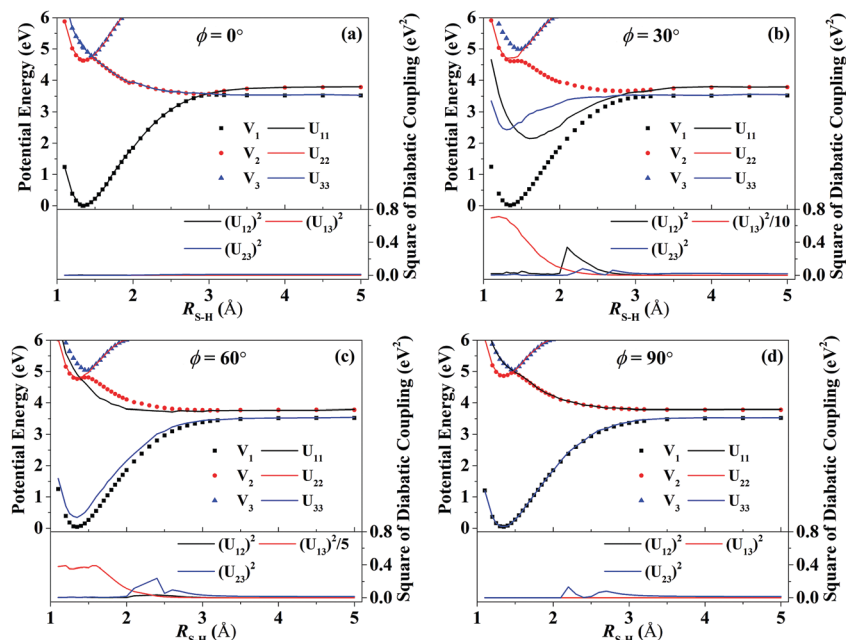


Fig. 8 Adiabatic ( $V_1$ ,  $V_2$ , and  $V_3$ ) and diabatic ( $U_{11}$ ,  $U_{22}$ , and  $U_{33}$ ) potential energy curves and the squares of the diabatic couplings ( $(U_{12})^2$ ,  $(U_{13})^2$ , and  $(U_{23})^2$ ) as functions of the stretching coordinate  $R$  for four values of the torsion angle  $\phi$  with the other geometric parameters fixed at the  $S_0$  equilibrium geometry.

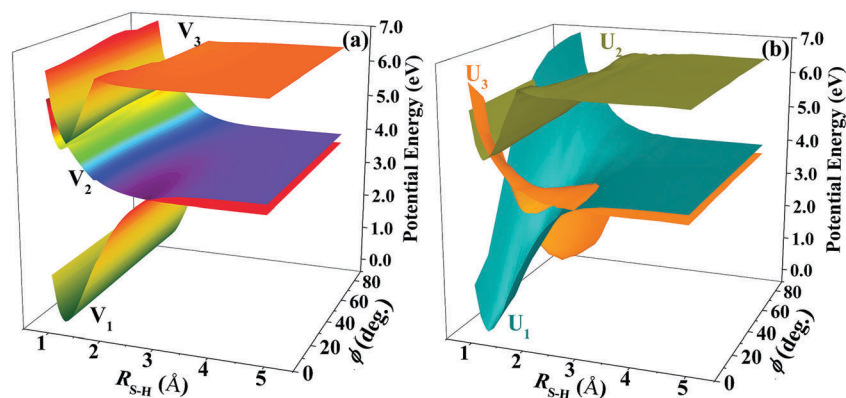


Fig. 9 Potential energy surfaces as functions of  $R$  and  $\phi$  with the other geometric parameters fixed at the  $S_0$  equilibrium geometry. (a) Adiabatic. (b) Diabatic.

even though adiabatic surfaces are well separated along  $\phi$  at small  $R$ . This nonintuitive diabatic crossing at geometries with well-separated adiabats is similar to what was seen in our previous study of thioanisole,<sup>83</sup> where a thorough discussion can be found. In Fig. 8,  $U_{13}$  is large at  $\phi = 30^\circ$  and  $60^\circ$  because the two adiabatic states are far apart while the two diabatic states are close due to the nonintuitive diabatic crossing.

It should be noticed that the figure shows that  $U_{12}$  and  $U_{23}$  undergo an abrupt increase around  $R = 2.1 \text{ \AA}$ , this is because  $V_3$

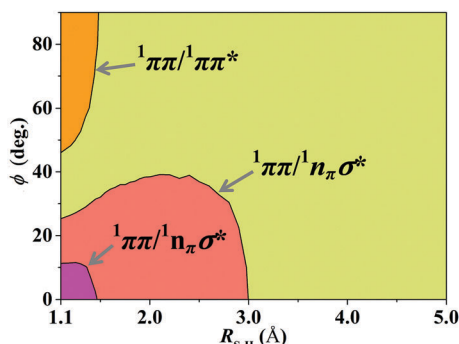


Fig. 10 Diabatic crossing seams calculated by model state diabaticization based on the fourfold way and XMC-QDPT adiabats. The  ${}^1\pi\pi^*/{}^1n_\pi\sigma^*$  ( $U_{22} = U_{33}$ ),  ${}^1\pi\pi/{}^1n_\pi\sigma^*$  ( $U_{11} = U_{33}$ ), and  ${}^1\pi\pi/{}^1\pi\pi^*$  ( $U_{11} = U_{22}$ ) seams are shown as projected onto the  $(R, \phi)$  two-dimensional plane.

crosses with an uncalculated higher state  $V_4$  which has a major configuration similar with one that prominent in the ground adiabatic state (it is a common occurrence in adiabatic-equivalent diabaticizations that there may be some unsmoothness due to the highest included adiabatic state having a crossing with the lowest non-included adiabatic state); however, the magnitudes of  $U_{12}$  and  $U_{23}$  are far smaller than the energy gap between the relevant states.

The three-dimensional adiabatic and diabatic potential energy surfaces are depicted in Fig. 9, from which we can see how the diabats cross. For an alternative mode of visualization, the diabatic crossing seams as functions of  $R$  and  $\phi$  can be projected onto the two-dimensional coordinate plane defined by  $(R, \phi)$ , and this is shown in Fig. 10. The  ${}^1\pi\pi^*/{}^1n_\pi\sigma^*$ ,  ${}^1\pi\pi/{}^1n_\pi\sigma^*$ , and  ${}^1\pi\pi/{}^1\pi\pi^*$  diabatic crossing seams correspond respectively to the hypersurfaces where  $U_{22} = U_{33}$ ,  $U_{11} = U_{33}$ , and  $U_{11} = U_{22}$ .

We have further explored the implications of the diabatic surfaces and their couplings in some other degrees of freedom. We calculated the diabatic energies and couplings by XMC-QDPT along Cartesian normal-mode displacements of the  $\nu_{16a}$  and  $\nu_{16b}$  out-of-plane ring distortion modes near two CIs. The vibrational displacements are obtained by M06-2X/aug-cc-pVTZ. Fig. 11 and 12 show the adiabatic and diabatic energy curves and the square of the 1–3 diabatic coupling  $(U_{13})^2$  (we use the notation  $U_{13}$  to denote  $H_{13}$  in the representation where  $\mathbf{H}$  is the diabatic electronic

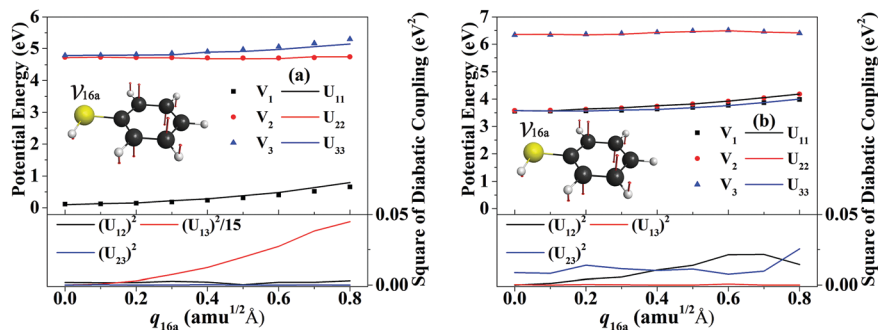


Fig. 11 The adiabatic ( $V_1$ ,  $V_2$ , and  $V_3$ ) and diabatic ( $U_{11}$ ,  $U_{22}$ , and  $U_{33}$ ) potentials and the squares of the diabatic couplings  $((U_{12})^2$ ,  $(U_{13})^2$ , and  $(U_{23})^2$ ) along mass-weighted Cartesian normal-mode displacements of the  $\nu_{16a}$  vibrational mode near the two CIs: (a)  $R = 1.45 \text{ \AA}$  and (b)  $3.00 \text{ \AA}$ .

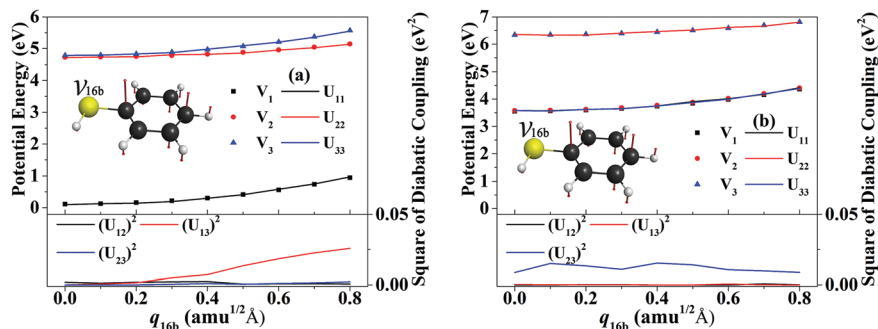


Fig. 12 The adiabatic ( $V_1$ ,  $V_2$ , and  $V_3$ ) and diabatic ( $U_{11}$ ,  $U_{22}$ , and  $U_{33}$ ) potentials and the squares of the diabatic couplings  $((U_{12})^2$ ,  $(U_{13})^2$ , and  $(U_{23})^2$ ) along mass-weighted Cartesian normal-mode displacements of the  $\nu_{16b}$  vibrational mode near the two CIs: (a)  $R = 1.45 \text{ \AA}$  and (b)  $3.00 \text{ \AA}$ . Note that in part b, the  $V_1$ ,  $V_2$ ,  $U_{11}$ , and  $U_{33}$  curves are almost on top of one another.

Hamiltonian, including nuclear repulsion). The smooth results in Fig. 11 and 12 are very encouraging, and they confirm the suitability of the fourfold-way for generating diabatic states even along significantly distorted paths that are far from planar equilibrium geometries. Furthermore Fig. 11a shows that, while both of these modes give negligible coupling near the second CI, mode  $\nu_{16a}$  is an important coupling mode near the first CI. This is encouraging in light of the inference from the experimental photofragment kinetic energy distribution<sup>12</sup> that the  $\nu_{16a}$  vibrational mode is among those observed to be excited but the  $\nu_{16b}$  vibrational mode is not.

## 4. Concluding remarks

Vertical excitation energies obtained by two wave function methods, QDPT and CR-EOM-CCSD(T) agree well with each other, and results in good agreement can also be obtained by Kohn–Sham density functional methods. We have simulated the electronic absorption spectrum of thiophenol by following a normal mode sampling approach. The result of the simulation is in excellent agreement with experiment, and it confirms that the strong peak in the spectrum mainly comes from the second  $^1\pi\pi^*$  transition ( $S_3 \leftarrow S_0$ ). The importance of the  $n(p_y)$  orbital of sulfur is shown by both the hole and the particle distributions based on KS-DFT wave functions and by the dominant configurations of CASSCF calculations.

Nonintuitive smooth diabatic potential energy surfaces of the lowest three singlet states were obtained as functions of the S–H stretching coordinate  $R$  and the C–C–S–H torsion coordinate  $\phi$  by XMC-QDPT using the fourfold way with the model-space diabaticization scheme. We determined the locations of the seams of diabatic crossings as functions of  $R$  and  $\phi$ .

To explore vibronic coupling near the two CIs, the diabatic energies and couplings were also calculated along Cartesian normal-mode displacements of two out-of-plane vibrational modes,  $\nu_{16a}$  and  $\nu_{16b}$ . The  $\nu_{16a}$  mode was shown to be an important coupling mode near the first CI.

## Conflicts of interest

There are no conflicts to declare.

## Acknowledgements

This work was supported in part by the U. S. Department of Energy, Office of Basic Energy Sciences, under grant no. DE-SC0008666, by National Natural Science Foundation of China (No. 51536002), and Linyao Zhang was also supported by a scholarship from China Scholarship Council (201706120185).

## References

- 1 A. L. Sobolewski and W. Domcke, *Chem. Phys. Lett.*, 1999, **315**, 293–298.
- 2 A. L. Sobolewski and W. Domcke, *Chem. Phys.*, 2000, **259**, 181–191.
- 3 A. L. Sobolewski and W. Domcke, *J. Phys. Chem. A*, 2001, **105**, 9275–9283.
- 4 A. L. Sobolewski, W. Domcke, C. Dedonder-Lardeux and C. Jouvet, *Phys. Chem. Chem. Phys.*, 2002, **4**, 1093–1100.
- 5 M. N. R. Ashfold, G. A. King, D. Murdock, M. G. D. Nix, T. A. A. Oliver and A. G. Sage, *Phys. Chem. Chem. Phys.*, 2010, **12**, 1218–1238.
- 6 G. M. Roberts and V. G. Stavros, *Chem. Sci.*, 2014, **5**, 1698–1722.
- 7 J. S. Lim, I. S. Lim, K. Lee, D. Ahn, Y. S. Lee and S. K. Kim, *Angew. Chem., Int. Ed.*, 2006, **45**, 6290–6293.
- 8 I. S. Lim, J. S. Lim, Y. S. Lee and S. K. Kim, *J. Chem. Phys.*, 2007, **126**, 34306.
- 9 J. S. Lim, H. Choi, I. S. Lim, S. B. Park, Y. S. Lee and S. K. Kim, *J. Phys. Chem. A*, 2009, **113**, 10410–10416.
- 10 A. L. Devine, M. G. D. Nix, R. N. Dixon and M. N. R. Ashfold, *J. Phys. Chem. A*, 2008, **112**, 9563–9574.
- 11 J. S. Lim, Y. S. Lee and S. K. Kim, *Angew. Chem., Int. Ed.*, 2008, **47**, 1853–1856.
- 12 M. N. R. Ashfold, A. L. Devine, R. N. Dixon, G. A. King, M. G. D. Nix and T. A. A. Oliver, *Proc. Natl. Acad. Sci. U. S. A.*, 2008, **105**, 12701–12706.
- 13 T. A. A. Oliver, Y. Zhang, M. N. R. Ashfold and S. E. Bradforth, *Faraday Discuss.*, 2011, **150**, 439–458.
- 14 Y. Zhang, T. A. A. Oliver, M. N. R. Ashfold and S. E. Bradforth, *Faraday Discuss.*, 2012, **157**, 141–163.
- 15 T. S. Venkatesan, S. G. Ramesh, Z. Lan and W. Domcke, *J. Chem. Phys.*, 2012, **136**, 174312.
- 16 T. A. A. Oliver, G. A. King, D. P. Tew, R. N. Dixon and M. N. R. Ashfold, *J. Phys. Chem. A*, 2012, **116**, 12444–12459.
- 17 H. Choi, Y. C. Park, Y. S. Lee, H. An and K. K. Baeck, *Chem. Phys. Lett.*, 2013, **580**, 32–36.
- 18 H. S. You, S. Han, J. S. Lim and S. K. Kim, *J. Phys. Chem. Lett.*, 2015, **6**, 3202–3208.
- 19 H. An, H. Choi, Y. S. Lee and K. K. Baeck, *ChemPhysChem*, 2015, **16**, 1529–1534.
- 20 V. Ovejas, M. Fernández-Fernández, R. Montero and A. Longarte, *Chem. Phys. Lett.*, 2016, **661**, 206–209.
- 21 B. Marchetti, T. N. V. Karsili, M. Cipriani, C. S. Hansen and M. N. R. Ashfold, *J. Chem. Phys.*, 2017, **147**, 13923.
- 22 G. Lin, C. Xie and D. Xie, *J. Phys. Chem. A*, 2017, **121**, 8432–8439.
- 23 G. Lin, C. Xie and D. Xie, *J. Phys. Chem. A*, 2018, **122**, 5375–5382.
- 24 S. L. Li, X. Xu and D. G. Truhlar, *Phys. Chem. Chem. Phys.*, 2015, **17**, 20093–20099.
- 25 M. Born and R. Oppenheimer, *Ann. Phys.*, 1927, **84**, 457–484.
- 26 D. G. Truhlar and C. A. Mead, *Phys. Rev. A: At., Mol., Opt. Phys.*, 2003, **68**, 32501.
- 27 E. Teller, *J. Phys. Chem.*, 1937, **41**, 109–116.
- 28 W. Lichten, *Phys. Rev.*, 1963, **131**, 229–238.
- 29 T. F. O'Malley, *Adv. At. Mol. Phys.*, 1971, **7**, 223–249.
- 30 V. Sidis and H. Lefebvre-Brion, *J. Phys. B: At. Mol. Phys.*, 1971, **4**, 1040–1054.
- 31 B. C. Garrett and D. G. Truhlar, *Theor. Chem.: Adv. Perspect.*, 1981, **6a**, 216–289.

- 32 B. K. Kendrick, C. A. Mead and D. G. Truhlar, *Chem. Phys.*, 2002, **277**, 31–41.
- 33 S. A. Evans, J. S. Cohen and N. F. Lane, *Phys. Rev. A: At., Mol., Opt. Phys.*, 1971, **4**, 2235–2248.
- 34 M. J. Redmon and D. A. Micha, *Int. J. Quantum Chem.*, 1974, **8**, 253–262.
- 35 L. R. Kahn, P. J. Hay and I. Shavitt, *J. Chem. Phys.*, 1974, **61**, 3530–3546.
- 36 R. W. Numrich and D. G. Truhlar, *J. Phys. Chem.*, 1975, **79**, 2745–2766.
- 37 C. Kubach and V. Sidis, *Phys. Rev. A: At., Mol., Opt. Phys.*, 1976, **14**, 152–161.
- 38 T. Van Voorhis, T. Kowalczyk, B. Kaduk, L.-P. Wang, C.-L. Cheng and Q. Wu, *Annu. Rev. Phys. Chem.*, 2010, **61**, 149–170.
- 39 H. Zhang, W. Wu and Y. Mo, *Comput. Theor. Chem.*, 2017, **1116**, 50–58.
- 40 H. Nakamura and D. G. Truhlar, *J. Chem. Phys.*, 2001, **115**, 10353–10372.
- 41 H. Nakamura and D. G. Truhlar, *J. Chem. Phys.*, 2002, **117**, 5576–5593.
- 42 H. Nakamura and D. G. Truhlar, *J. Chem. Phys.*, 2003, **118**, 6816–6829.
- 43 K. R. Yang, X. Xu and D. G. Truhlar, *Chem. Phys. Lett.*, 2013, **573**, 84–89.
- 44 H.-J. Werner and W. Meyer, *J. Chem. Phys.*, 1981, **74**, 5794–5801.
- 45 M. W. Schmidt and M. S. Gordon, *Annu. Rev. Phys. Chem.*, 1998, **49**, 233–266.
- 46 S. L. Li, D. G. Truhlar, M. W. Schmidt and M. S. Gordon, *J. Chem. Phys.*, 2015, **142**, 064106.
- 47 H. Nakano, *J. Chem. Phys.*, 1993, **99**, 7983–7992.
- 48 H. Nakano, *Chem. Phys. Lett.*, 1993, **207**, 372–378.
- 49 A. A. Granovsky, *J. Chem. Phys.*, 2011, **134**, 214113.
- 50 K. R. Yang, X. Xu, J. Zheng and D. G. Truhlar, *Chem. Sci.*, 2014, **5**, 4661–4680.
- 51 K. R. Yang, X. Xu and D. G. Truhlar, *J. Chem. Theory Comput.*, 2014, **10**, 924–933.
- 52 E. B. Wilson, *Phys. Rev.*, 1934, **45**, 706–714.
- 53 Y. Zhao and D. G. Truhlar, *Theor. Chem. Acc.*, 2008, **120**, 215–241.
- 54 A. D. Boese and N. C. Handy, *J. Chem. Phys.*, 2002, **116**, 9559–9569.
- 55 Y. Zhao and D. G. Truhlar, *J. Chem. Phys.*, 2006, **125**, 194101.
- 56 H. S. Yu, X. He, S. L. Li and D. G. Truhlar, *Chem. Sci.*, 2016, **7**, 5032–5051.
- 57 A. D. Becke, *Phys. Rev. A: At., Mol., Opt. Phys.*, 1988, **38**, 3098–3100.
- 58 C. T. Lee, W. T. Yang and R. G. Parr, *Phys. Rev. B: Condens. Matter Mater. Phys.*, 1988, **37**, 785–789.
- 59 B. Miehlich, A. Savin, H. Stoll and H. Preuss, *Chem. Phys. Lett.*, 1989, **157**, 200–206.
- 60 A. D. Becke, *J. Chem. Phys.*, 1993, **98**, 5648–5652.
- 61 B. J. Lynch, Y. Zhao and D. G. Truhlar, *J. Phys. Chem. A*, 2003, **107**, 1384–1388.
- 62 T. H. Dunning Jr., *J. Chem. Phys.*, 1989, **90**, 1007–1023.
- 63 D. E. Woon and T. H. Dunning Jr., *J. Chem. Phys.*, 1993, **98**, 1358–1371.
- 64 T. H. Dunning Jr., K. A. Peterson and A. K. Wilson, *J. Chem. Phys.*, 2001, **114**, 9244–9253.
- 65 A. Schäfer, C. Huber and R. Ahlrichs, *J. Chem. Phys.*, 1994, **100**, 5829–5835.
- 66 M. E. Casida, in *Recent Advances in Density Functional Methods, Part I*, ed. D. P. Chong, World Scientific, Singapore, 1995, pp. 155–192.
- 67 I. Tamm, *J. Phys. (USSR)*, 1945, **9**, 449.
- 68 S. M. Dancoff, *Phys. Rev.*, 1950, **78**, 382.
- 69 S. Hirata and M. Head-Gordon, *Chem. Phys. Lett.*, 1999, **314**, 291–299.
- 70 H. Koch and P. Jorgensen, *J. Chem. Phys.*, 1990, **93**, 3333–3344.
- 71 J. F. Stanton and R. J. Bartlett, *J. Chem. Phys.*, 1993, **98**, 7029–7039.
- 72 K. Kowalski and P. Piecuch, *J. Chem. Phys.*, 2004, **120**, 1715–1738.
- 73 K. Kowalski, *J. Chem. Phys.*, 2009, **130**, 194110.
- 74 H. J. Silverstone and O. Sinanoglu, *J. Chem. Phys.*, 1966, **44**, 1899–1907.
- 75 A. V. Marenich, C. J. Cramer and D. G. Truhlar, *J. Phys. Chem. B*, 2009, **113**, 6378–6396.
- 76 E. Cancès, B. Mennucci and J. Tomasi, *J. Chem. Phys.*, 1997, **107**, 3032–3041.
- 77 B. Mennucci, E. Cancès and J. Tomasi, *J. Phys. Chem. B*, 1997, **101**, 10506–10517.
- 78 M. Caricato, B. Mennucci, J. Tomasi, F. Ingrosso, R. Cammi, S. Corni and G. Scalmani, *J. Chem. Phys.*, 2006, **124**, 124520.
- 79 H. Köppel, J. Gronki and S. Mahapatra, *J. Chem. Phys.*, 2001, **115**, 2377–2388.
- 80 H. Köppel and B. Schubert, *Mol. Phys.*, 2006, **104**, 1069–1079.
- 81 G. J. Atchity and K. Ruedenberg, *Theor. Chem. Acc.*, 1997, **97**, 47–58.
- 82 X. Xu, K. R. Yang and D. G. Truhlar, *J. Chem. Theory Comput.*, 2013, **9**, 3612–3625.
- 83 S. L. Li, X. Xu, C. E. Hoyer and D. G. Truhlar, *J. Phys. Chem. Lett.*, 2015, **6**, 3352–3359.
- 84 M. J. Frisch, G. W. Trucks, H. B. Schlegel, G. E. Scuseria, M. A. Robb, J. R. Cheeseman, G. Scalmani, V. Barone, G. A. Petersson, H. Nakatsuji, X. Li, M. Caricato, A. V. Marenich, J. Bloino, B. G. Janesko, R. Gomperts, B. Mennucci, H. P. Hratchian, J. V. Ortiz, A. F. Izmaylov, J. L. Sonnenberg, D. Williams-Young, F. Ding, F. Lipparini, F. Egidi, J. Goings, B. Peng, A. Petrone, T. Henderson, D. Ranasinghe, V. G. Zakrzewski, J. Gao, N. Rega, G. Zheng, W. Liang, M. Hada, M. Ehara, K. Toyota, R. Fukuda, J. Hasegawa, M. Ishida, T. Nakajima, Y. Honda, O. Kitao, H. Nakai, T. Vreven, K. Throssell, J. A. Montgomery, Jr., J. E. Peralta, F. Ogliaro, M. J. Bearpark, J. J. Heyd, E. N. Brothers, K. N. Kudin, V. N. Staroverov, T. A. Keith, R. Kobayashi, J. Normand, K. Raghavachari, A. P. Rendell, J. C. Burant, S. S. Iyengar, J. Tomasi, M. Cossi, J. M. Millam, M. Klene, C. Adamo, R. Cammi, J. W. Ochterski, R. L. Martin, K. Morokuma, O. Farkas,

- J. B. Foresman and D. J. Fox, *Gaussian 16, Revision A.03*, Gaussian, Inc., Wallingford CT, 2016.
- 85 M. S. Gordon and M. W. Schmidt, in *Theory and Applications of Computational Chemistry: The First Forty Years*, ed. C. E. Dykstra, G. Frenking, K. S. Kim and G. E. Scuseria, 2005, pp. 1167–1189.
- 86 H. A. Witek, Y. K. Choe, J. P. Finley and K. Hirao, *J. Comput. Chem.*, 2002, **23**, 957–965.
- 87 M. Valiev, E. J. Bylaska, N. Govind, K. Kowalski, T. P. Straatsma, H. J. Van Dam, D. Wang, J. Nieplocha, E. Apra and T. L. Windus, *Comput. Phys. Commun.*, 2010, **181**, 1477–1489.
- 88 J. Zheng, Z.-H. Li, A. W. Jasper, D. A. Bonhommeau, R. Valero, R. Meana-Pañeda, S. L. Mielke and D. G. Truhlar, *ANT 2017*, University of Minnesota, Minneapolis, 2017, <http://comp.chem.umn.edu/ant>.
- 89 T. Lu and F. Chen, *J. Comput. Chem.*, 2012, **33**, 580–592.
- 90 F. J. A. Ferrer, J. Cerezo, E. Stendardo, R. Improta and F. Santoro, *J. Chem. Theory Comput.*, 2013, **9**, 2072–2082.